Intranuclear cascade-percolation approach for protons and light fragments production in neon-niobium reactions at 400 and 800 MeV per nucleon

G. Montarou, J. Marroncle,* J. P. Alard, J. Augerat, N. Bastid, P. Charmensat, P. Dupieux,
L. Fraysse, M. J. Parizet, and A. Rahmani[†]
Laboratoire de Physique Corpusculaire,
Université Blaise Pascal, IN2P3-CNRS, Clermont-Ferrand, F-63177 Aubière Cedex, France

R. Babinet, C. Cavata, M. Demoulins, H. Fanet, J. Gosset, D. L'Hôte, M. C. Lemaire,
B. Lucas, J. Poitou, and O. Valette
Service de Physique Nucleaire, DAPNIA, CE-Saclay, F-91191 Gif-sur-Yvette Cedex, France

F. Brochard, P. Gorodetzky, and C. Racca
Centre de Recherches Nucléaires, 23 rue du Loess, BP 20 CR, 67037 Strasbourg, France

J. Cugnon
Institut de Physique, Université de Liège, Sart Tilman, B-4000 Liège 1, Belgium
(Received 23 July 1992)

The results of intranuclear cascade calculations (ideal gas with two-body collisions and no mean field), complemented by a simple percolation procedure, are compared with experimental data on protons and light nuclear fragments (d, t, ^{3}He, and ^{4}He) measured in 400 and 800 MeV/nucleon Ne+Nb collisions using a large solid angle detector. The model reproduces quite well global experimental observables like nuclear fragment multiplicity distributions or production cross sections, and nuclear fragment to proton ratios. For rapidity distributions the best agreement occurs for peripheral reactions. Transverse momentum analysis confirms once again that the cascade, although being a microscopic approach, gives too small a collective flow, the best agreement being reached for $Z=2$ nuclear fragments. Nevertheless these comparisons are encouraging for further improvements of the model. Moreover, such an approach is easy to extend to any other models that could calculate the nucleon phase space distribution after the compression stage of the reaction, when light nuclear fragments emitted at large angles are constructed from percolation.

PACS number(s): 25.70.Pq

I. INTRODUCTION

Intermediate-energy heavy-ion collisions offer the unique opportunity to infer the properties of nuclear matter at high density and temperature which are probed in the early stage of these collisions. For incident projectile energies of a few hundred MeV per nucleon, the speed of interpenetration of the two colliding nuclei exceeds the sound velocity in ordinary nuclear matter so that nuclear matter is highly compressed up to densities $\simeq 2-3$ times the normal nuclear density ρ_0 and excited to temperatures $\simeq 50-100$ MeV. After the phase of compression, the system then expands and cools down, tending to lower densities and temperatures.

The formation of the nuclear fragments at the final stage of these reactions depends on the nucleons phase space distribution at this final time. As this distribution is directly determined by the dynamical evolution of the system during the collision, the nuclear fragment production is governed not only by the initial conditions of the collision (incident energy, impact parameter), but also by the properties of the highly excited nuclear matter. This relation has been used [1–3] to derive experimentally from the observed nuclear fragment yields the entropy per nucleon produced in the reaction, i.e., one of the intensive thermodynamic variables of the nuclear equation of state.

In order to calculate the final phase space distribution, one needs a nuclear transport model. Many transport models [4] describe heavy-ion collisions at intermediate energy within the mean-field approximation and are adequate to describe the dynamical evolution up to the time of the reaction when fragmentation occurs. Afterwards, nuclear fragment formation can be predicted using percolation [5]. For example Ngô *et al.* have developed a specific percolation model, the "restructured aggregation model" [6], coupled to a Landau-Vlasov equation [7], in order to predict experimental nuclear fragment charge distribution in O+AgBr reactions between 50 and 200 MeV/nucleon [8]. As far as the problem of cluster formation is concerned, it has been proposed to replace

mean-field dynamical approaches by nuclear transport models which are more suitable to calculate the N-body phase space distribution. Such a method has been already used for predictions in the multifragmentation regime, using intranuclear cascade (INC) [9,10], or quantum molecular dynamic (QMD) [11,12]. In this paper we use an equivalent procedure to predict light nuclear fragment production in 400 and 800 MeV/nucleon Ne+Nb reactions. The nuclear transport model used in order to describe the dynamic of the early phase of the collision is the Liège intranuclear cascade. From this nuclear transport model, we determine the phase space distribution at the end of the reaction, when light nuclear fragments are constructed by a simple percolation approach, followed by a deexcitation process. This procedure can be viewed as an extension of the method used in Ref. [13] for deuteron cross-section predictions in α+Pb, Cu, and C reactions between 200 and 800 MeV/nucleon.

This paper is organized as follows. Section II will be devoted to the presentation of the model. In order to check the validity of this model, we compare it to experimental data measured with the 4π detector DIOGENE in a Ne+Nb reaction at 400 and 800 MeV/nucleon. Section III will briefly recall the characteristics of the detector and describe the data analysis procedure. A systematic comparison of the predictions of the model with experimental observables will be presented in Sec. IV. The features of these comparisons will lead to a discussion of the model in Sec. V.

II. THE MODEL

A. Intranuclear cascade (INC) model

The basic assumption of the Liège intranuclear cascade model [14] is that the collision of the two nuclei can be described as a succession of free nucleon-nucleon collisions. For each colliding nucleus (projectile or target), the initial nucleon positions are randomly distributed inside a sphere of radius $1.12A^{1/3}$, where A is the mass number of the nucleus.

The initial nucleon momenta are uniformly distributed inside a Fermi sphere with radius $p_F = 270$ MeV/c. Then the projectile nucleus is boosted toward the target nucleus with the beam velocity so that the velocity of each nucleon is the sum of the nucleus velocity and the individual Fermi motion. But in order to avoid a spurious expansion of the two nuclei before the reaction, the nucleons of the system are frozen until they have their first interaction. Specifically, the Fermi momentum of each nucleon is recorded and then given back to it just before its first interaction. In the following analysis, we consider only "participant" nucleons, defined as nucleons which underwent at least one collision with another nucleon during the reaction. The remaining nucleons, defined as the "spectators," are out of the scope of this analysis.

The original code has been improved since a prescription is used for the Pauli blocking factor: The number of particles is counted in a sphere which is centered at the final phase space coordinates of the colliding pairs, with a radius of 2 fm in coordinate space and 200 MeV/c in

momentum space. So we can determine the occupation factor f by examining the neighborhood of the final-state phase space whenever a collision would occur; the collision is allowed with the probability $(1-f)$. Furthermore, the isospin dependence of the elementary nucleon-nucleon cross sections is taken into account, and both nn or np total elastic and inelastic cross sections are parametrized in order to reproduce the experimental standard data.

Moreover, a binding potential V has been implemented so that the nucleons are considered as initially moving in potential wells, providing a binding field to the initial nuclei. The binding potential is introduced with the relation

$$E^2 = p^2 + (m+V)^2 , \qquad (1)$$

where $V = -32$ MeV and m is the nucleon mass $(m = 938$ MeV).

We consider here collisions between neon projectile and niobium target nucleus at 400 and 800 MeV incident kinetic energy per nucleon. For each projectile energy, the impact parameter varies in 10 steps from 0 to $9b_{max}/9.5$, where b_{max} is equal to $R_{Ne} + R_{Nb}$. For each value of b, we have simulated 1500 and 1300 collisions at 400 and 800 MeV/nucleon, respectively.

B. Percolation

The cascade process is stopped at the time t_F, defined as the time when the system is freely expanding: t_F is equal to 50 fm/c for both 400 and 800 MeV/nucleon reactions. Afterwards a percolation procedure is applied to the final r-space distribution of the nucleons: We decide that two nucleons belong to the same cluster if their relative distance in r space is smaller than some "percolation distance" r_{per}. An expression of r_{per} at the final time t_F is given by

$$r_{per} = r_d + \frac{p_0}{m}(t_F - t_{FO}) , \qquad (2)$$

where t_{FO} is the "freeze-out" time, r_d the deuteron radius $(r_d = 2$ fm), and p_0 a limit on the relative momentum of the nucleons in the fragment. The times t_{FO} are determined for each impact parameter as follows. In the energy domain considered here, the time evolution of the cumulated number of baryon-baryon collisions shows a steady increase and then suddenly flattens. We choose t_{FO} as the time at which the cumulated number of nucleon-nucleon collisions reaches $\frac{2}{3}$ of its final value. The momentum distribution does not change drastically after t_{FO} since the remaining collisions are soft, t_{FO} is equal to 18 fm/c (15 fm/c) for the most central 800 MeV/nucleon (400) collisions. It goes down to 9 fm/c for the most peripheral collision $(b = 9b_{max}/9.5)$ at both energies. As t_{FO} is dependent on b/b_{max}, r_{per} is in the same way a function of the impact parameter of the collision. Finally, our simple model depends upon only one parameter, i.e., the limit on the relative momentum p_0 of the nucleons in the fragment. The value of p_0 is determined by requiring the best agreement between the global exper-

imental and predicted cluster-to-proton ratios (d/p, t/p, and ^{3,4}H/p). The best values of p_0 have been found to be equal to 210 and 260 MeV/c for 400 and 800 MeV/nucleon collisions. One can quote that these values are close to the Fermi momentum p_F and that the small variation going from the 400 MeV/nucleon to the 800 MeV/nucleon case may simply reflect a corresponding uncertainty in the cluster formation time.

Concretely, at the final time of the cascade process, t_F, the clustering algorithm grows a minimal spanning tree [15] based on the relative distance between nucleons in r space by successively adjoining the nearest remaining nucleon to a partially formed tree until all "participant" nucleons are attached to the final tree. After, we remove inconsistent edges with length larger than r_{per}. Clusters will result from groups of neighboring nucleons (subtrees) which have small edges. But some of them consist only of an isolated nucleon as shown in Fig. 1.

C. Deexcitation

We have to keep in mind that clusters are until now defined on a purely geometrical prescription. Consequently, the clustering algorithm can produce unstable clusters. Some of these prefragments are totally unphysical and are immediately rejected. The remaining prefragments are excited, and we calculate their excitation energy in the following way. Each produced prefragment is characterized by a total momentum equal to the total momentum of the center of mass of the constituent nucleons:

$$\mathbf{P}_{frag} = \sum_{i=1}^{A} \mathbf{p}_i \ , \tag{3}$$

where the $\mathbf{p}_i$ are the nucleon individual momenta. Then we suppose that the excitation of the prefragment is given by the total energy of the A nucleons minus the total energy of the prefragment E_t, calculated from $\mathbf{P}_{frag}$ and the mass of this prefragment. This mass is taken from the stable of isotopes [16] for mass number less or equal to 16 and calculated with a macroscopic formula [17] otherwise. The excitation energy E^* of a prefragment could be written as

$$E^* = \sum_{i=1}^{A} (\mathbf{p}_i^2 + m^2)^{1/2} - E_t \ , \tag{4}$$

where m is the nucleon mass. The disassembly of the prefragments in their center-of-mass frame is idealized as a two-stage process: a fast explosion into light- and medium-mass fragments, followed by sequential evaporation from the explosion products. In the evaporation stage, only p, n, and ^{4}He emissions are considered. The treatment of the two stages depends on the excitation energy of the prefragment and is based on the Fai-Randrup statistical model [17], i.e., on the assumption that explosion or evaporation populates phase space statistically and in invoking a grand canonical ensemble approximation of the exact microcanonical phase space.

III. EXPERIMENTAL SETUP AND DATA ANALYSIS

The experimental distributions used in the present analysis have been measured with the large solid angle detector DIOGENE [18] at the Saturne II synchrotron in Saclay. As shown in Fig. 2, the central part of the DIOGENE facility consists of a pictorial drift chamber (PDC), with cylindrical symmetry, inside a 1-T constant magnetic field. Since the performances of the detector affect directly the experimental observables, it is necessary to take into account the experimental biases which deform these observables. Most of these biases result directly from the PDC acceptance. A particle can be registered in the PDC only if it is emitted at a polar angle with respect to the beam direction larger than $\sim 15°$ and smaller than $\sim 140°$, and if it has enough energy to exit from target and cross the internal beam pipe. This internal beam pipe was a cylindrical 1.5-mm-thick (1.18-g/cm^2) 10-cm-diam stainless-steel pipe for the 400 MeV/nucleon collisions and was subsequently replaced for the 800 MeV/nucleon collisions by a 2-mm-thick carbon fiber pipe (0.45 gm/cm^2) to improve the resolution and reduce the low-energy cut. The resolution on the momentum (p) and the polar (θ) and azimuthal (ϕ) emission angles of the particle detected in the PDC also determine the effective acceptance of the detector. When θ becomes smaller than 30° or larger than 120°, the resolutions on momentum and emission angle rapidly
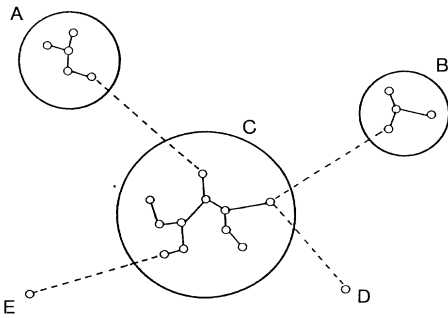

FIG. 1. Construction of the minimum spanning tree from the graph of the distances of nucleons in r space at the final time of the reaction t_F. Dashed lines indicate the removed edges with length larger than r_{per}. Final subtrees result in clusters (A, B, and C) or isolate nucleons (D and E).
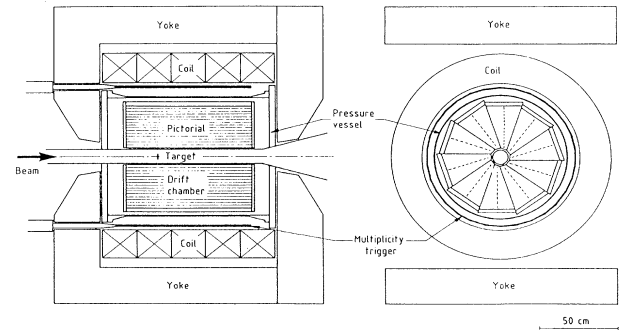

FIG. 2. Schematic views of the pictorial drift chamber of the DIOGENE facility: longitudinal (left view) and transverse (right view) sections.

deteriorate. At 90° the resolutions are dominated by the target thickness. Typical values [full width at half maximum (FWHM)] for protons are $\Delta p/p \sim 20\%$ and of the order of a few degrees for $\Delta\phi$ and $\Delta\theta$. The PDC acceptance can be parametrized in the (y,η) plane, where y stands for the particle rapidity and η is its transverse momentum divided by its mass. All of the following analysis has been done with the PDC acceptance reported in Tables I and II for both energies.

A barrel-shaped set of 30 plastic scintillators slabs surrounds the PDC. The trigger of the PDC requires that at least 2 among the 30 scintillators slabs have been hit during the reaction and that no beam-velocity highly charged particles be detected downstream from the target. A charged particle can reach one of the scintillator slabs if it has enough energy to cross the 4-mm-thick iron PDC pressure vessel and if it is emitted at a polar angle between $\sim 40°$ and $\sim 120°$. The corresponding acceptance of these scintillators slabs is reported in Table III for pions and baryons. Consequently, DIOGENE is well suited to investigate the "participant" region, since the trigger provides a bias against most peripheral collisions and only fragments formed from "participants" nucleons are measured in the PDC acceptance.

The PDC allows us to record in the three dimensions the trajectory of any lightly charged particle emitted within the acceptance. Ionization electrons, induced by the passage of the particle in the gas of the PDC, drift under the action of the homogeneous electric field to a radial plane of multiplying wires parallel to the beam axis, where the energy loss and the three coordinates of the particle trajectory are sampled.

Identification of the particles is achieved using the correlation between the particle magnetic rigidity and the mean energy loss in the gas of the PDC. A particle-

TABLE I. PDC acceptance for protons, deuterons, tritons, ^{3}He, and ^{4}He for the 400 MeV/nucleon reactions (1.5-mm-thick steel internal beam pipe). θ is the polar angle, y the rapidity, and η the transverse momentum divided by the mass.

	$132° > \theta > 20°$	
p	$y < -0.05$	$\eta > 0.312 + 0.595y$
	$-0.05 < y < 0$	$\eta > 0.310$
	$y > 0$	$\eta > 0.310 - 0.617y$
d	$y < -0.033$	$\eta > 0.237 + 0.458y$
	$-0.033 < y < 0$	$\eta > 0.247$
	$y > 0$	$\eta > 0.235 - 0.551y$
t	$y < -0.03$	$\eta > 0.195 + 0.404y$
	$-0.03 < y < 0$	$\eta > 0.228$
	$y > 0$	$\eta > 0.207 - 0.551y$
^{3}He	$y < -0.052$	$\eta > 0.302 + 0.338y$
	$-0.052 < y < 0$	$\eta > 0.324$
	$y > 0$	$\eta > 0.324 - 0.588y$
^{4}He	$y < -0.038$	$\eta > 0.299 + 0.504y$
	$-0.038 < y < 0$	$\eta > 0.305$
	$y > 0$	$\eta > 0.294 - 0.558y$

TABLE II. PDC acceptance for protons, deuterons, tritons, ^{3}He, and ^{4}He for the 800 MeV/nucleon reactions (2-mm-thick carbon fiber internal beam pipe). θ is the polar angle, y the rapidity, and η the transverse momentum divided by the mass.

	$132° > \theta > 20°$	
p	$y < -0.032$	$\eta > 0.240 + 0.467y$
	$-0.032 < y < 0$	$\eta > 0.286$
	$y > 0$	$\eta > 0.239 - 0.619y$
d	$y < -0.032$	$\eta > 0.197 + 0.564y$
	$-0.032 < y < 0$	$\eta > 0.228$
	$y > 0$	$\eta > 0.197 - 0.668y$
t	$y < -0.025$	$\eta > 0.171 + 0.505y$
	$-0.025 < y < 0$	$\eta > 0.195$
	$y > 0$	$\eta > 0.171 - 0.650y$
^{3}He	$y < -0.037$	$\eta > 0.262 + 0.337y$
	$-0.037 < y < 0$	$\eta > 0.287$
	$y > 0$	$\eta > 0.264 - 0.513y$
^{4}He	$y < -0.036$	$\eta > 0.236 + 0.500y$
	$-0.036 < y < 0$	$\eta > 0.279$
	$y > 0$	$\eta > 0.253 - 0.572y$

identification plot is presented in Fig. 3. The (π,p) separation is excellent, and the (p,d) separation is good. Heavier particle identification is affected by the experimental uncertainty on p/Z, which results from uncertainties on the coordinates of the measured points of the tracks and from multiple scattering in the target, the internal beam pipe, and the gas of PDC and by statistical fluctuations of the energy loss in the gas of the PDC.

The process of off-line analysis was done by a specific program [19] which deals with the track reconstruction, the particle identification, and the computation, for each particle, of its momentum vector and the associated uncertainties.

In such an electronic device, the double-track resolution affects the PDC efficiency since electronic dead time results in missed hits as the particle multiplicity in the chamber increases. Specifically, when the multiplicity of charged particles emitted in the PDC acceptance is larger than 10, some of them cannot be measured by the detector so that the measured multiplicity is lower than the real one. We take into account such distortions by means of a simulation program which computes the complete response of the detector and its connected electronics to each cascade-percolation simulated event and is used as an "experimental filter" for the model calculation. The track reconstruction algorithm distorts the experimental

TABLE III. Scintillator slab barrel acceptance for pions and baryons.

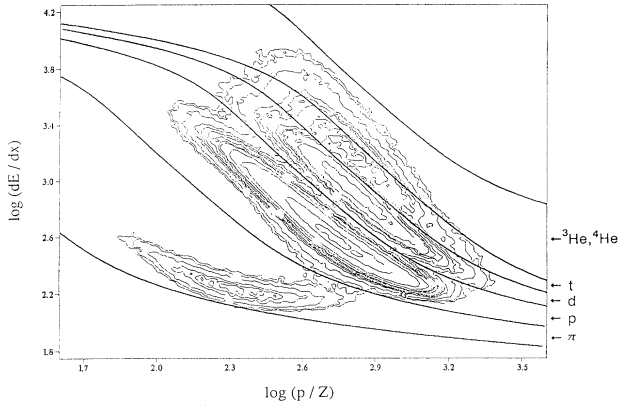|	$119° > \theta > 37°$	
	$y > 0$	$y < 0$
π	$\eta > 0.81 - 0.33y$	$\eta > 0.81 + 0.33y$
Baryons	$\eta > 0.41 - 0.40y$	$\eta > 0.41 + 0.30y$

FIG. 3. $\langle dE/dX \rangle_T$ versus p/Z identification scatter plot, obtained in Ne+Nb collisions for particles detected in the PDC. The mean truncated energy loss per unit length, $\langle dE/dX \rangle_T$, is calculated from the samples of $\langle dE/dX \rangle$ measured along the trajectory of the particle in the PDC. The magnetic rigidity p/Z is obtained from the transverse curvature radius and the polar emission angle of the particle. The lines indicate the limits used in off-line analysis for particle separation.

observables in the same way as the detector facility does; the simulated events are then treated by the track reconstruction and analysis program as real events. In this way experimental biases are realistically taken into account so that the comparison between experimental and theoretical events can be achieved with a complete confidence.

Such a large solid angle detector offers an ideal opportunity to select central collisions. The impact parameter selection is based on the correlation between the centrality of the collision and the total nuclear charge multiplicity $M_{\tilde{p}}$ measured in the PDC acceptance:

$$M_{\tilde{p}} = M_p + M_d + M_t + 2(M_{^3He} + M_{^4He}) , \tag{5}$$

where M_p, M_d, M_t, $M_{^3He}$, and $M_{^4He}$ are the proton, deuteron, tritium, ^{3}He, and ^{4}He multiplicities measured in the PDC acceptance as defined in Tables I and II. The more central the collision is, the higher $M_{\tilde{p}}$ is. The experimental $M_{\tilde{p}}$ multiplicity distribution is compared to the cascade-percolation prediction for both 400 and 800 MeV/nucleon reactions in Fig. 4. Our model reproduces
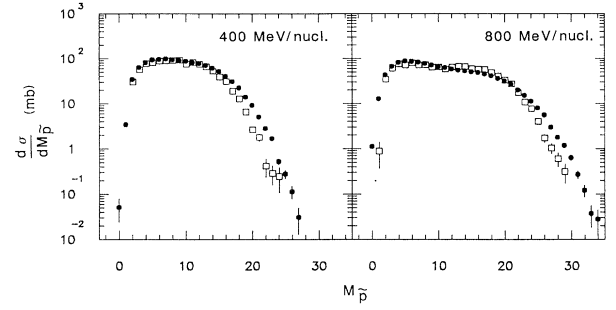

FIG. 4. $M_{\tilde{p}}$ multiplicity distribution for 400 and 800 MeV/nucleon Ne+Nb collisions. $M_{\tilde{p}}$ is defined by Eq. (5). Cascade-percolation predictions correspond to open symbols and experimental data to solid symbols.

rather well these $M_{\tilde{p}}$ multiplicity distributions, except for the high multiplicity tail of the spectra, for which the experimental multiplicity cross sections are systematically underestimated by the cascade-percolation model. Nevertheless, this figure indicates that the number of "participant" nucleons, used in the impact parameter determination, is correctly estimated by the model.

The selection can be presented as a function of the squared reduced impact parameter $\tilde{b}^2 = b^2/(R_{Ne} + R_{Nb})^2$, where b stands for the impact parameter and R_{Ne} and R_{Nb} are the radii of the Ne and Nb nuclei, respectively. The quantity $\tilde{b}^2$ is estimated from the $M_{\tilde{p}}$ distribution as the ratio of the integrated cross section to the geometrical one, with the integration starting from the highest multiplicity bin and assuming a one-to-one correspondence between the increasing impact parameter and decreasing multiplicity [20]. The geometrical cross section of the reaction is given by the expression

$$\sigma_0 = \pi r_1^2 (A_{Ne}^{1/3} + A_{Nb}^{1/3})^2 , \tag{6}$$

with $r_1 = 1.2$ fm, and A_{Ne} and A_{Nb} are the projectile and target atomic numbers. Such a method has been used in the present analysis in order to select specific impact parameter windows. Each of these windows is associated with a class of events selected via a $M_{\tilde{p}}$ multiplicity interval and, consequently, to a mean-square reduced impact parameter ($\langle \tilde{b} \rangle_{expt}$) as reported in Table IV.

TABLE IV. Definition of the specific classes of events corresponding to peripheral and central reactions. For each range of $M_{\tilde{p}}$, $\langle \tilde{b}^2 \rangle_{expt}$ is the mean-square reduced impact parameter estimated from the experimental $M_{\tilde{p}}$ multiplicity distribution. The mean-square reduced impact parameter has been also determined for the cascade-percolation simulated events: $\langle \tilde{b}^2 \rangle_B$ is estimated from the simulated $M_{\tilde{p}}$ distribution; $\langle \tilde{b}^2 \rangle_A$ is calculated directly from the reduced impact parameter distribution of the cascade-percolation events (Fig. 5). The average standard deviations of the distribution of $\tilde{b}_A^2$ for cascade-percolation events are indicated in parentheses.

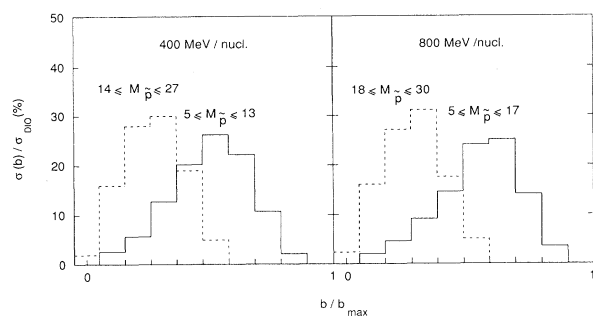| $M_{\tilde{p}}$ | 400 MeV/nucleon | | 800 MeV/nucleon | |
	Central [14–27]	Peripheral [5–13]	Central [18–30]	Peripheral [5–17]
$\langle \tilde{b}^2 \rangle_{expt}$	0.05	0.29	0.04	0.31
$\langle \tilde{b}^2 \rangle_A$	0.09 (0.07)	0.275 (0.16)	0.09 (0.07)	0.31 (0.17)
$\langle \tilde{b}^2 \rangle_B$	0.04	0.26	0.05	0.30

FIG. 5. Total reaction cross-section distribution in the trigger acceptance versus reduced impact parameter for 400 and 800 MeV/nucleon Ne+Nb simulated collisions. Solid lines correspond to peripheral collisions and the dashed lines to central collisions. These distributions are renormalized to the total reaction cross section in the trigger acceptance (σ_{DIO}).

In order to test it, we applied our impact parameter determination to the cascade-percolation simulated events. Since we know exactly the impact parameter of the simulated events, one can plot, as shown in Fig. 5, the reduced impact parameter distribution of the events corresponding to a specific range of the $M_{\tilde{p}}$ multiplicity and calculate in the same time the associated mean-square reduced impact parameter corresponding to this distribution. These values ($\langle \tilde{b}^2 \rangle_A$) are also reported in Table IV, where they are compared to those estimated only from the simulated $M_{\tilde{p}}$ distribution ($\langle \tilde{b}^2 \rangle_B$). The largest difference between $\langle \tilde{b}^2 \rangle_A$ and $\langle \tilde{b}^2 \rangle_B$ occurs for central collisions, at both 400 and 800 MeV/nucleon. Moreover,

Fig. 5 shows that the selection of the impact parameter of the collision by means of $M_{\tilde{p}}$ is only qualitative since square reduced impact parameter distributions are characterized by large fluctuations.

IV. EXPERIMENTAL RESULTS AND COMPARISON WITH THE MODEL

The comparison of experimental results and model predictions will be made now starting from the global variables and getting to more and more sophisticated observables. In all the following figures, solid symbols correspond to experimental data and open squares to the cascade-percolation calculations. The error bars depict statistical errors only.

A. Multiplicity distributions

In Figs. 6 and 7 are represented the multiplicity distributions of p, d, t, and $Z=2$ nuclear fragments. The experimental p and d distributions are well reproduced over the whole multiplicity range. On the other hand, these figures show that the high multiplicity tail of the triton and $Z=2$ nuclear fragment spectra are underpredicted by the cascade-percolation calculation. In Table V are reported the total nuclear charge and fragment production cross sections. These values indicate that the 400 meV/nucleon cross sections are systematically underestimated by the model. At 800 MeV/nucleon the experimental cross sections are correctly reproduced by the cascade-percolation predictions.
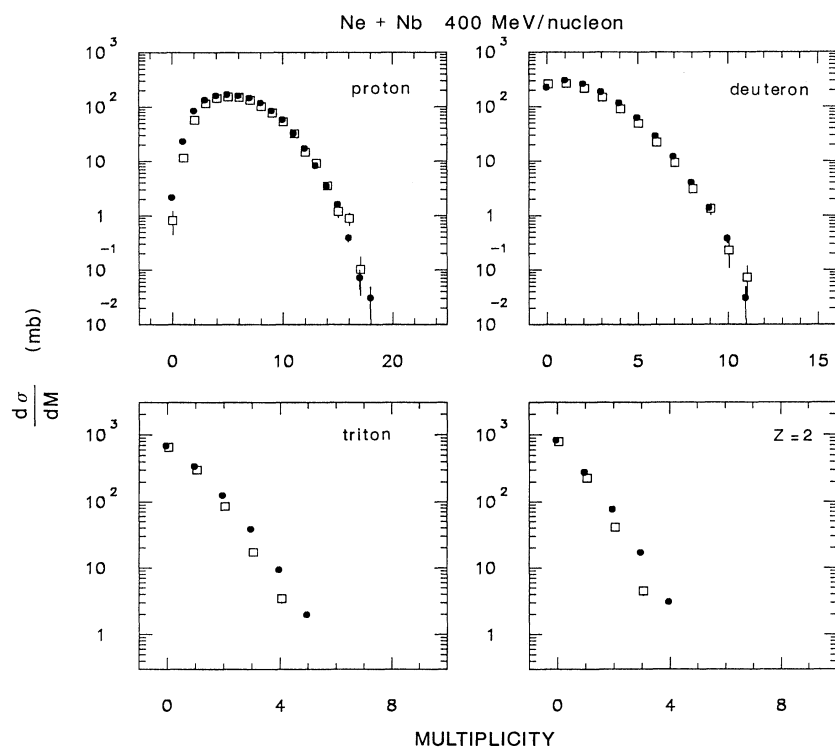

FIG. 6. Multiplicity distributions of protons, deuterons, tritons, and $Z=2$ nuclear fragments emitted in 400 MeV/nucleon Ne+Nb collisions. Solid circles, experiment; open squares, cascade-percolation predictions.
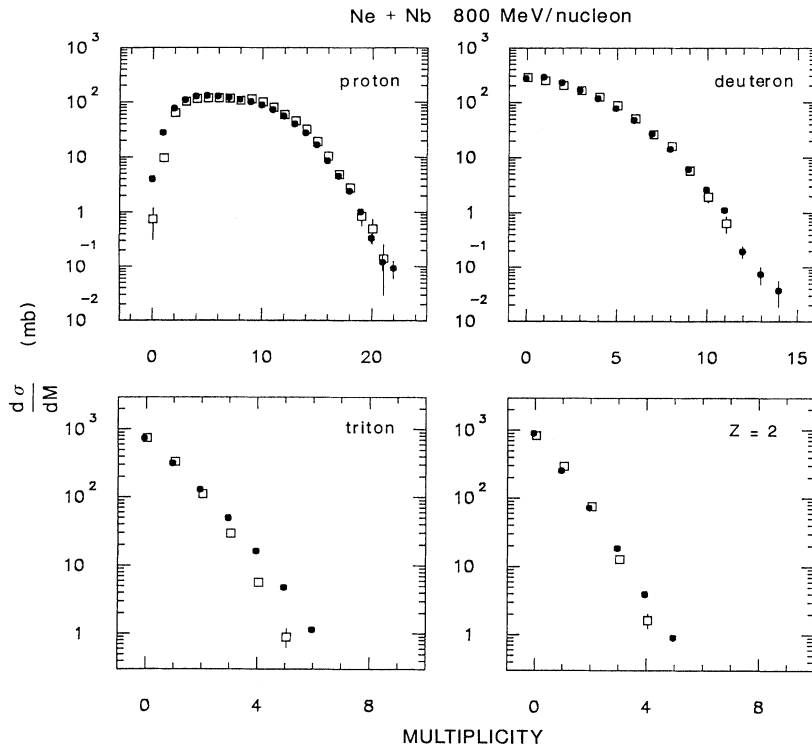
FIG. 7. Multiplicity distributions of protons, deuterons, tritons, and $Z=2$ nuclear fragments emitted in 800 MeV/nucleon Ne+Nb collisions. Solid circles, experiment; open squares, cascade-percolation predictions.

B. Cluster-to-proton ratios

Figure 8 represents the comparison of the experimental and theoretical variation of the main cluster-to-proton ratios, i.e., d/p, t/p, ^{3}He/p, and ^{4}He/p, versus $M_{\bar{p}}$. The agreement between predicted and experimental d/p is very good for high multiplicity $M_{\bar{p}}$ events; it deteriorates at low multiplicity. On the contrary the agreement between experimental and predicted t/p, ^{3}He/p, and ^{4}He/p ratios is better for low $M_{\bar{p}}$ events. These figures show that the experimental ratios, especially in the case of the heavier fragments, are qualitatively better reproduced by the cascade percolation for the 800 MeV/nucleon reaction.

C. Rapidity distributions

The rapidity distributions of baryons [21] could be used in order to infer some understanding of the dynamic

TABLE V. Experimental σ_{expt} and predicted σ_{INC} total nuclear charge and fragment cross section in the PDC acceptance. Experimental values are affected by a $\sim 15\%$ systematic error.

	400 MeV/nucleon		800 MeV/nucleon	
	σ_{expt} (mb)	σ_{INC} (mb)	σ_{expt} (mb)	σ_{INC} (mb)
$\bar{p}$	11 383	9664	13 438	13 588
p	7150	6482	8870	9136
d	2480	1991	2800	2797
t	759	541	816	669
$Z=2$	497	325	476	493

behavior of the collision. Specifically, the nuclear stopping power is characterized by the longitudinal momentum degradation length of the projectile nucleons in the target nucleus. This degradation length is directly related to the mean free path $\lambda = 1/(\rho\sigma_{\text{eff}})$ of the nucleons, where σ_{eff} is the effective nucleon-nucleon cross section in a nuclear medium at density ρ.

Rapidity distributions of p, d, t, and $Z=2$ nuclear fragments are shown in the Figs. 9 and 10 for central and in Figs. 11 and 12 for peripheral collisions. The best agreement between experimental and predicted distributions occurs rather in peripheral collisions except for the 800 MeV/nucleon $Z=2$ nuclear fragment distribution, which seems to be simply shifted toward higher rapidity values.

For central collisions, the experimental and predicted rapidity distributions agree only for the proton distribution at 800 MeV/nucleon. For the heavier fragments, the simulated rapidity distribution is systematically shifted toward higher rapidity values; the larger shift appears for the $Z=2$ nuclear fragment distribution. This could be an indication that the degradation of the initial longitudinal momentum of the projectile nucleons is not properly reproduced by the model. This effect is reduced for 400 MeV/nucleon, which can be related to the fact that, at this energy, the nucleon-nucleon cross section is at its minimum and still largely only elastic.

For central as well as for peripheral reactions, the experimental rapidity distributions peak at some different rapidities, depending on the nature of the particle. But, as shown in Table I or II, the PDC acceptance is also dependent on the nature of the particle, especially the

low-energy cut. If the phase domain corresponding to low η values is densely populated, these different acceptances could explain such an effect.

These figures also show that, at 400 as well as 800 MeV/nucleon, the experimental or predicted rapidity distributions peak at rapidity values which are not very much dependent upon the centrality of the reaction. But, as stated before, the correspondence between the impact parameter of the collision and the multiplicity of nuclear
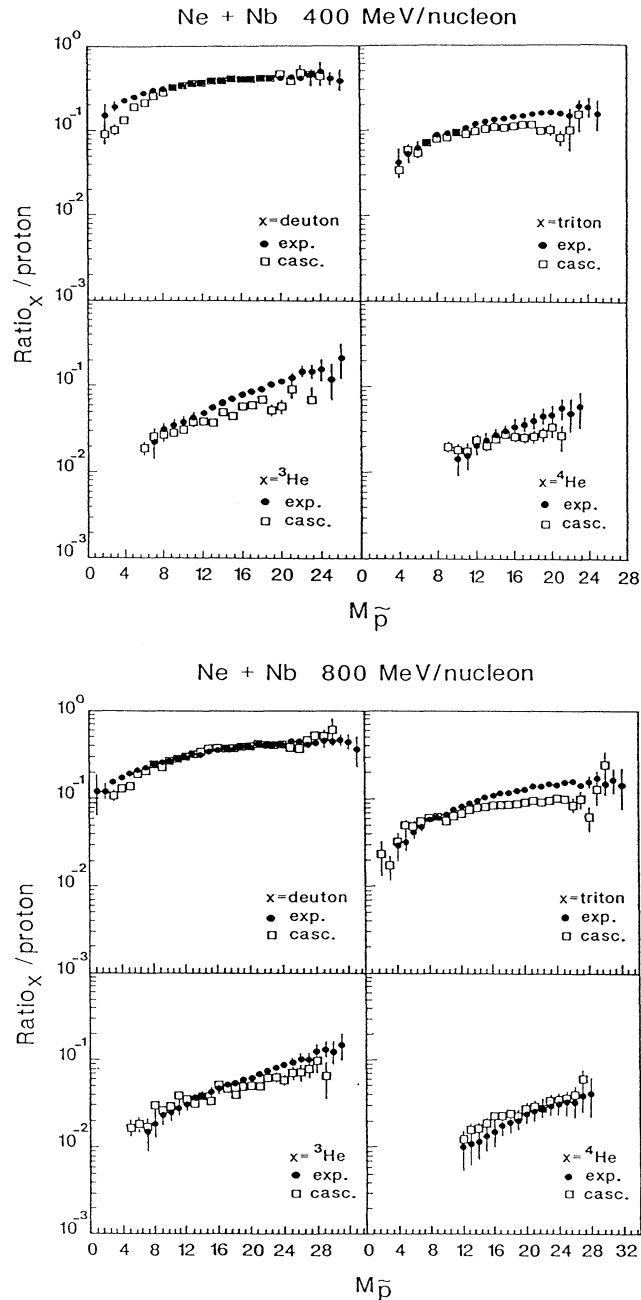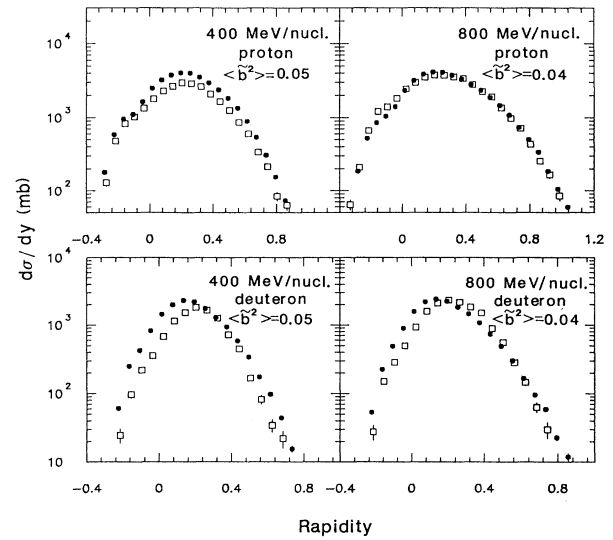
FIG. 9. Rapidity distributions of protons and deuterons emitted in central 400 and 800 MeV/nucleon Ne+Nb collisions. Solid circles, experiment; open squares, cascade-percolation predictions.

charged particles detected in the PDC acceptance is only qualitative since, as shown in Fig. 5, to a specific value of $M_{\tilde{p}}$ corresponds a large range of reduced impact parameters. Moreover, we have to keep in mind that particles are detected only in a limited part of 4π sr and that the PDC angular acceptance cuts out the high rapidity part of the distributions, which is presumably dominant for the most peripheral reactions in such an asymmetrical reaction.

FIG. 8. Variation of d/p, t/p, $^3He/p$, and $^4He/p$ ratios versus $M_{\tilde{p}}$ for 400 and 800 MeV/nucleon Ne+Nb collisions. Solid circles, experiment; open squares, cascade-percolation predictions.
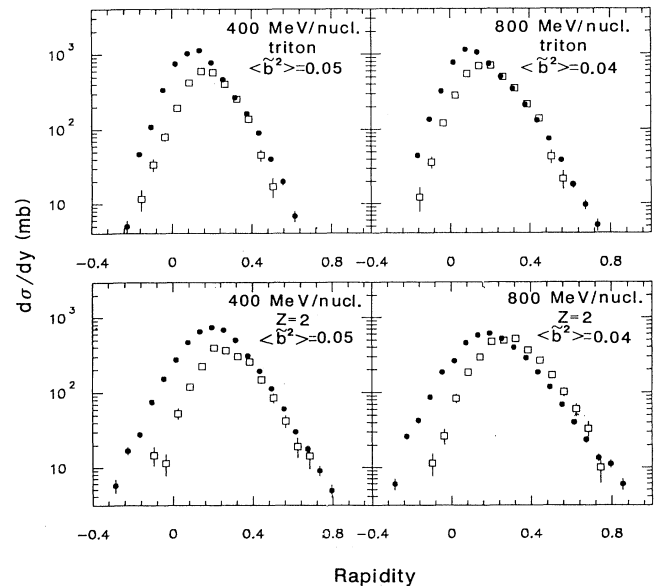
FIG. 10. Rapidity distributions of tritons and $Z=2$ nuclear fragments emitted in central 400 and 800 MeV/nucleon Ne+Nb collisions. Solid circles, experiment; open squares, cascade-percolation predictions.
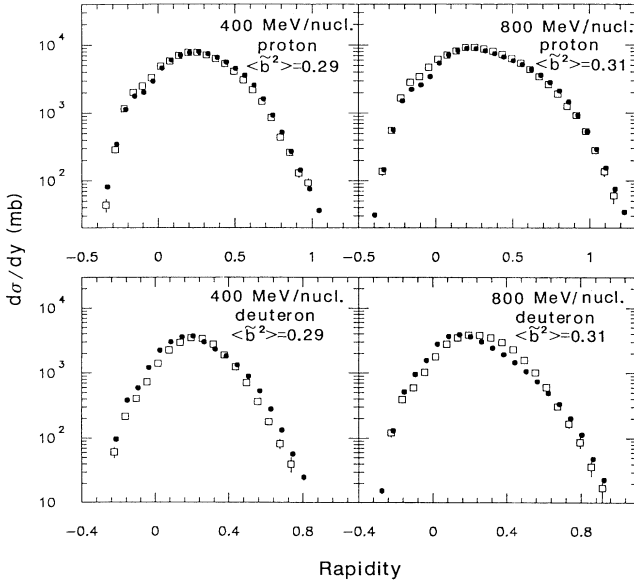
FIG. 11. Rapidity distributions of protons and deuterons emitted in peripheral 400 and 800 MeV/nucleon Ne+Nb collisions. Solid circles, experiment; open squares, cascade-percolation predictions.

If the incident projectile nucleus is completely stopped in the target nucleus, one can obtain a thermalized nuclear "fireball" [22]. Such an equilibrium occurs when λ is small compared to the overall size of the system, so that the nucleons of the projectile could undergo several collisions. Assuming that the "fireball" velocity in the laboratory frame, β_F, depends only on the relative number of "participant" nucleons coming from the projectile (n_p) and the target (n_t), β_F is given by the expression [22]

$$\beta_F = \frac{n_p[t(t+2m')]^{1/2}}{n_p t + (n_p + n_t)m'} , \tag{7}$$

where t is the projectile incident kinetic energy per nucleon and m' is the mass of a bound nucleon (taken to be 931 MeV). n_p and n_t values are estimated on a very simple geometrical prescription, assuming that the "participant" nucleons are contained in the volume of the projectile and target nuclei delimited by mutual clean cylindrical cuts of the two nuclear spheres. Using the impact parameter values reported in the Table IV, corresponding to central collisions, we obtain the "fireball" rapidity $y_F = \tanh^{-1}\beta_F = 0.29$ for 400 MeV/nucleon and $y_F = 0.40$ for 800 MeV/nucleon central collisions.

For all kinds of particles, the discrepancy between the experimental or the cascade-percolation predicted rapidity distributions and the clean-cut "fireball" mean rapidity is larger at 800 MeV/nucleon than at 400 MeV/nucleon. At 400 MeV/nucleon, the best agreement occurs for protons and $Z=2$ nuclear fragments since the experimental rapidity distributions peak at $y \sim 0.24$ instead of $y_F = 0.29$. At 800 MeV/nucleon, the experimental or the cascade-percolation predicted rapidity distributions are by no mean consistent with this simple "fireball" model since the rapidity distributions peak at values very much smaller than the "fireball" one.

D. Double-differential cross sections

In order to present the comparison between experimental and predicted double-differential cross sections, we choose two variables such that, for a Boltzmann distribution of particles emitted by a single source, double-differential cross sections come to a simple analytic expression [23]. These variables are the rapidity y and the dimensionless variable $(\gamma_\perp)$ related to the transverse momentum $p_\perp$ and to the mass m of the particle by

$$\gamma_\perp = \left[\frac{p_\perp^2}{m^2} + 1\right]^{1/2} . \tag{8}$$

The rapidity is a variable which transforms additively by a Lorentz transformation parallel to the beam direction, and $\gamma_\perp$ is invariant under such transformations. In the case of a thermalized source of particles at "temperature" T_0, the invariant Boltzmann distribution can be expressed, in the rest frame of the source, as

$$\frac{d^2N}{2\pi m^2 \gamma_\perp dy \, d\gamma_\perp} = \frac{N\gamma_\perp \cosh(y)}{4\pi m^2 C} \exp\left[-\frac{\gamma_\perp \cosh(y)}{\gamma_0}\right] . \tag{9}$$

γ_0 is the reduced "temperature" defined as T_0/m, and C is a constant term equal to

$$C = \gamma_0[K_0(1/\gamma_0) + 2\gamma_0 K_1(1/\gamma_0)] , \tag{10}$$

where K_0 and K_1 are the usual MacDonald functions [24]. In the laboratory frame where the source rapidity is y_0, the distribution transforms as
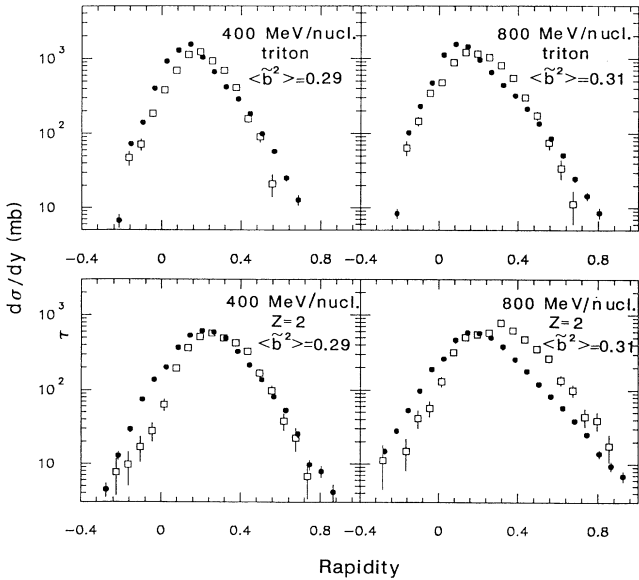

FIG. 12. Rapidity distributions of tritons and $Z=2$ nuclear fragments emitted in peripheral 400 and 800 MeV/nucleon Ne+Nb collisions. Solid circles, experiment; open squares, cascade-percolation predictions.

$$\frac{d^2N}{2\pi m^2 \gamma_\perp dy\, d\gamma_\perp}$$

$$= \frac{N\gamma_\perp \cosh(y - y_0)}{4\pi m^2 C} \exp\left[-\frac{\gamma_\perp \cosh(y - y_0)}{\gamma_0}\right]. \quad (11)$$

Finally, we can write a cross section, which is invariant by a Lorentz transformation parallel to the beam, as

$$\frac{1}{\gamma_\perp^2}\frac{d^2N}{d\gamma_\perp dy} = \frac{N}{2C}\cosh(y - y_0)\exp\left[-\frac{\gamma_\perp \cosh(y - y_0)}{\gamma_0}\right]$$

$$= N_{\mathrm{eff}}(y)\exp\left[-\frac{\gamma_\perp}{T_{\mathrm{eff}}(y)}\right], \quad (12)$$

where $N_{\mathrm{eff}}(y) = \cosh(y - y_0)N/2C$ and $T_{\mathrm{eff}}(y)$ $= \gamma_0 \cosh(y - y_0)$. For any rapidity, the double-differential cross section $(1/\gamma_\perp^2)d^2N/d\gamma_\perp dy$ is simply an exponential defined by the two quantities N_{eff} and T_{eff}, which, in the case of emission by a single thermalized source, are related by

$$N_{\mathrm{eff}}T_{\mathrm{eff}} = N\gamma_0/2C . \quad (13)$$

Even if this last condition is not completely fulfilled, one can evaluate, using Eq. (12), the deviation of the experimental distribution from a Boltzmann distribution. But the main advantage of this parametrization results from the characterization of the spectra by the variation of the parameters $T_{\mathrm{eff}}(y)$ and $N_{\mathrm{eff}}(y)$ versus rapidity.

Figures 13–15 represent the double-differential cross sections $(1/\gamma_\perp^2)d^2N/d\gamma_\perp dy$ for p, d, and $Z = 2$ nuclear fragments. In these figures, experimental data are compared to the cascade-percolation predictions for different rapidity bins. Unfortunately, the event statistic is not sufficient to define, even for protons, such double-differential distributions corresponding to central or peripheral selected reactions. Because of the $2\pi b$ geometrical weight of each event, these spectra are rather representative of peripheral collisions. In order to make these plots understandable, the values corresponding to the second curve starting from the top are divided by a factor of 10, and each subsequent curve is divided by a further factor of 10. For all the spectra, the first points corresponding to the lowest $\gamma_\perp$ values are widely affected by the acceptance of the PDC. Beyond this shoulder, experimental and theoretical cross sections follow straight lines in the semilogarithmic plots so that, as claimed above, these distributions can be summarized by the characteristic parameters $T_{\mathrm{eff}}(y)$ and $N_{\mathrm{eff}}(y)$.

For proton spectra, the predicted data are very close to experimental ones when $\gamma_\perp \lesssim 1.4$. For $\gamma_\perp \gtrsim 1.4$, we observe some disagreement between the experimental and predicted spectra, especially for the four last rapidity intervals $(y \geq 0.4)$ of 800 MeV/nucleon distributions, where the statistic is sufficient in the high-$\gamma_\perp$ part of the spectra to achieve full comparisons. Nevertheless, the first experimental points, corresponding to the main contributions to the total cross section, are correctly reproduced by the model. In 400 MeV/nucleon distributions, the cross-section values corresponding to $\gamma_\perp \geq 1.4$ are not very significative since they are affected by large error
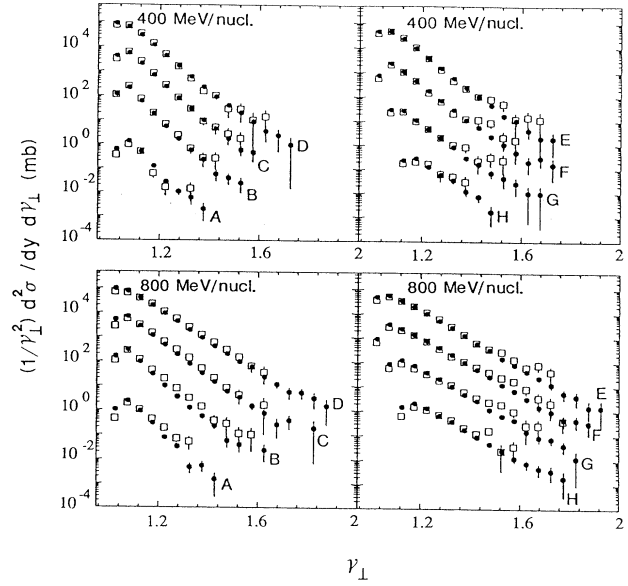

FIG. 13. Proton double-differential cross sections $(1/\gamma_\perp^2)d^2\sigma/d\gamma_\perp dy$ versus $\gamma_\perp$ for 400 and 800 MeV/nucleon Ne + Nb collisions for different rapidity intervals. Curves labeled A correspond to $-0.4 \leq y < -0.2$, B to $-0.2 \leq y < 0$, C to $0 \leq y < 0.2$, D to $0.2 \leq y < 0.4$, E to $0.4 \leq y < 0.6$, F to $0.6 \leq y < 0.8$, G to $0.8 \leq y < 1.0$, and H to $1.0 \leq y < 1.2$. In order to make these plots understandable, the values corresponding to the second curve starting from the top are divided by a factor 10, and each subsequent curve is divided by a further factor of 10.
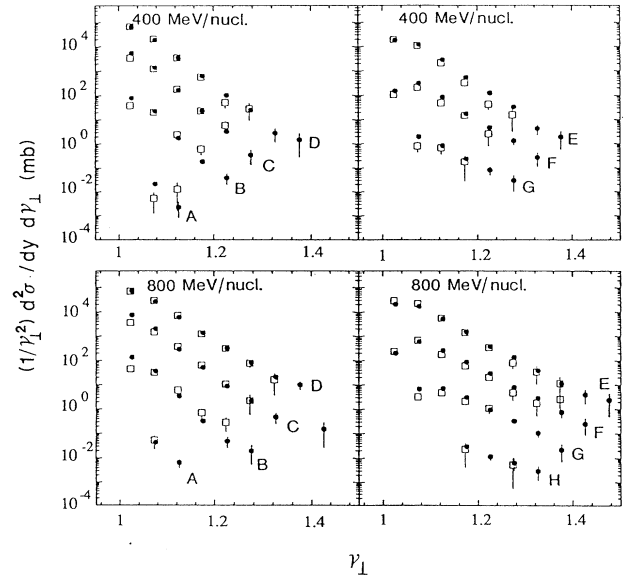
FIG. 14. Deuteron double-differential cross sections $1/\gamma_\perp^2 d^2\sigma/d\gamma_\perp dy$ versus $\gamma_\perp$ for 400 and 800 MeV/nucleon Ne + Nb collisions for different rapidity intervals as defined in Fig. 13.
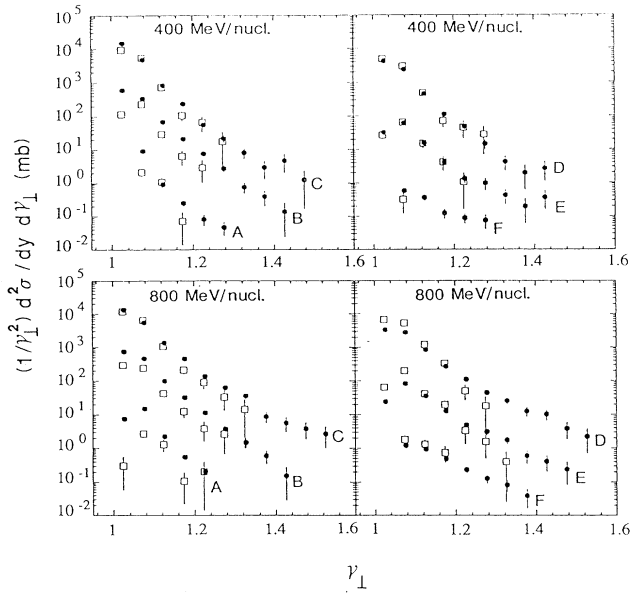
FIG. 15. $Z = 2$ nuclear fragment double-differential cross sections $1/\gamma_\perp^2 d^2\sigma/d\gamma_\perp dy$ versus $\gamma_\perp$ for 400 and 800 MeV/nucleon Ne + Nb collisions for different rapidity intervals. Curves labeled A correspond to $-0.2 \leq y < 0$, B to $0 \leq y < 0.2$, C to $0.2 \leq y < 0.4$, D to $0.4 \leq y < 0.6$, E to $0.6 \leq y < 0.8$, and F to $0.8 \leq y < 1.0$. In order to make these plots understandable, the values corresponding to the second curve starting from the top are divided by a factor of 10, and each subsequent curve is divided by a further factor of 10.

bars. Figure 15 shows that, at 800 MeV/nucleon, the $Z = 2$ nuclear fragment predicted rapidity distribution is shifted toward higher rapidities with respect to the experimental one, since the model overpredicts the first points of the experimental cross section in the rapidity bins E and D ($0.4 \leq y \leq 0.8$) and underpredicts the experimental distribution in the rapidity bins A and B ($-0.2 \leq y \leq 0.2$). Such a deviation already appears in the global rapidity distribution shown in Fig. 12. Nevertheless, it seems that the part of the spectra corresponding to larger $\gamma_\perp$ values is correctly reproduced.

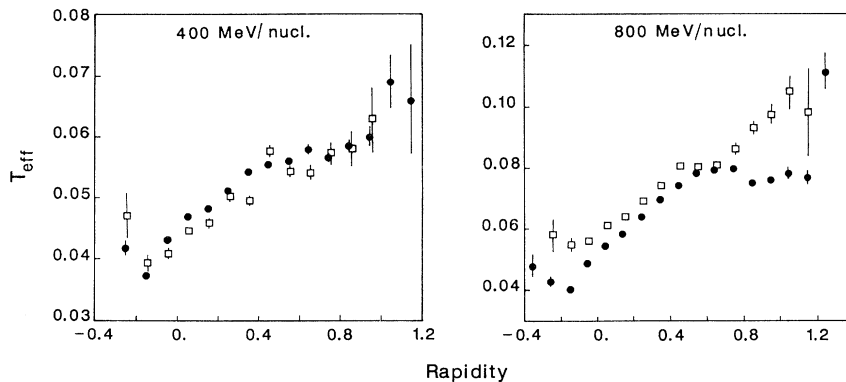The characteristic parameters $T_{\text{eff}}(y)$ and $N_{\text{eff}}(y)$ are

calculated by a fit of the high-$\gamma_\perp$ part of the spectra. But instead of $N_{\text{eff}}(y)$, we determine $N_G(y)$, which is the ordinate of the fitted spectra at $\gamma_\perp$ equal to 1. This artifice minimizes the correlation between the slope and the ordinate of the fitted straight lines. This is because N_{eff} is the ordinate at the unphysical value $\gamma_\perp = 0$, which is far from the physical region and hence very sensitive to small deviations in the fit. Moreover, these characteristic parameters are also very sensitive to the systematic errors of the particle spectra.

Figures 16 and 17 represent the variation of $T_{\text{eff}}(y)$ versus rapidity for protons and deuterons. Figure 16 shows that for the protons the experimental T_{eff} values saturate at 800 MeV/nucleon for high rapidities. So this figure confirms what has been observed in the Fig. 13 for the high rapidity part of the 800 MeV/nucleon experimental spectra, but also indicates that for the lower rapidity values the same kind of discrepancy appears. Figure 17 shows that the $T_{\text{eff}}(y)$ values extracted from deuteron experimental spectra are in a rather good agreement with the predicted corresponding values. At same rapidity value, deuteron T_{eff} values are about a factor of 2 below the proton ones, as expected from a thermal model from the deuteron to proton mass ratio.

Figures 18 and 19 represent the variation of $N_G(y)$ versus rapidity, and Fig. 20 represents the $N_{\text{eff}}T_{\text{eff}}$ product for protons. This product is not at all constant as a function of the rapidity. At 800 MeV/nucleon, its variation is 10 times larger that at 400 MeV/nucleon. Nevertheless, for the 400 MeV/nucleon reaction the predicted $N_{\text{eff}}T_{\text{eff}}$ product agrees quite well with the experimental one. For the 800 MeV/nucleon reaction, we observe again a disagreement between experimental and predicted values of the product for lowest and highest rapidities. We cannot conclude immediately, from these figures, that this is evidence of a nonthermalized source since, in order to have sufficient statistic, the parameters T_{eff} and N_{eff} have been extracted from spectra without any M_p selection, i.e., for a large range of the impact parameter and, consequently, for a large range of the source velocities. Moreover, we suppose that the source has no radial expression during the reaction: Such a radial velocity could affect widely the expression of the distribution of the emitted particles [Eqs. (11)–(13)].

FIG. 16. Variation of T_{eff} versus rapidity for proton spectra.
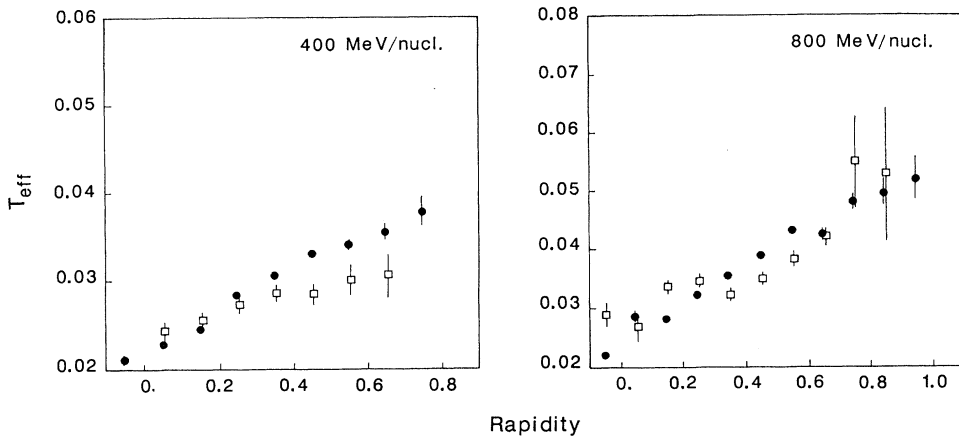
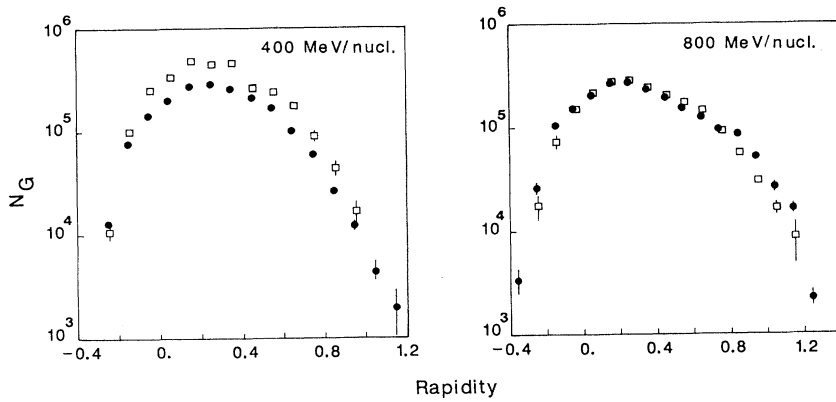FIG. 17. Variation of T_{eff} versus rapidity for deuteron spectra.

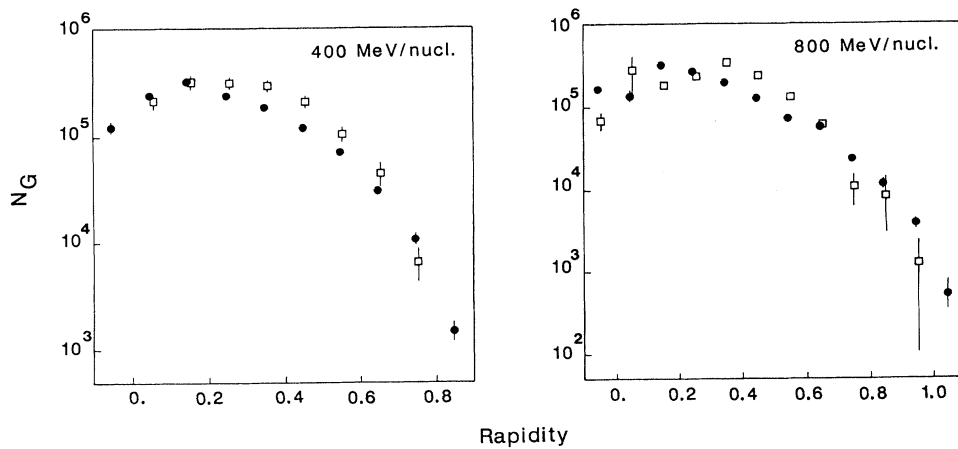FIG. 18. Variation of N_G versus rapidity for proton spectra.

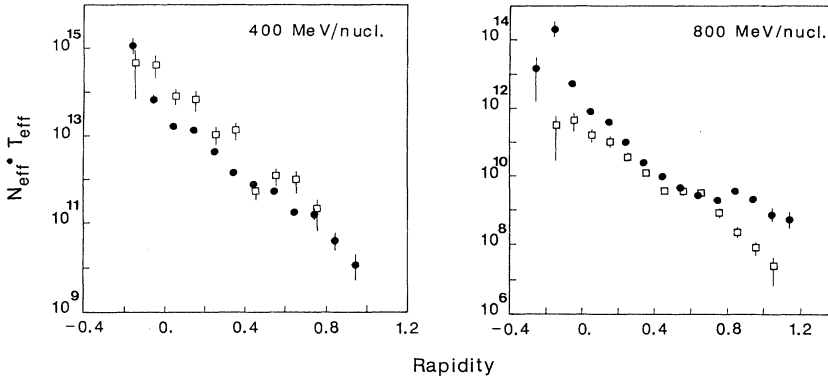FIG. 19. Variation of N_G versus rapidity for deuteron spectra.

FIG. 20. Variation of $N_{\rm eff}T_{\rm eff}$ versus rapidity for proton spectra.

E. Transverse momentum analysis

On the basis of simple hydrodynamic assumptions, a shock wave phenomenon was predicted to occur in high-energy heavy-ion collisions [25]. Hydrodynamic models predict a strong azimuthal correlation of particles emitted from the reaction zone as a direct signature of such a fluidlike behavior of the nuclear matter [26]. This strong azimuthal correlation of particles has been experimentally unambiguously established since results of 4π detectors have revealed two different collective effects occurring in the reaction plane: first, a large azimuthal asymmetric emission of "participant" particles, the "side splash," and second, a sideward deflection of "spectator" particles, the "bounce off" due to transverse communication with the reaction zone. Moreover, an enhanced flow of particles perpendicular to the reaction plane, the "squeeze out," has also been observed [27].

The Danielewicz-Odyniec [28] transverse momentum analysis method has been widely used in order to analyze experimental data in terms of collective flow variables. In each single event, the azimuth of the reaction plane is estimated from the multiparticle information. Concretely, the reaction plane is constructed individually for each single particle μ from the transverse momentum components $\mathbf{p}_{\perp}$ of all remaining particles of the same event:

$$\mathbf{Q}(\mu) = \sum_{\nu \neq \mu} \mathbf{p}_{\perp}(\nu)\omega(\nu) , \tag{14}$$

where $\omega(\nu)$ is the weight factor of particle ν, which we take as

$$\omega(\nu) = y(\nu) - \langle y \rangle , \tag{15}$$

with $\langle y \rangle = \sum_{\mu} A(\mu)y(\mu)/\sum_{\mu}A(\mu)$, where $A(\mu)$ is the mass number of particle μ. Such a definition of $\mathbf{Q}(\mu)$ ensures that autocorrelations are removed. The transverse momentum vector of the particle μ is projected onto the estimated reaction plane by evaluating the scalar product:

$$p_x(\mu) = \mathbf{p}_{\perp}(\mu) \cdot \frac{\mathbf{Q}(\mu)}{|\mathbf{Q}(\mu)|} , \tag{16}$$

yielding the average of the in-plane transverse momentum $\langle p_x \rangle$. This transverse momentum analysis can be done for each species of light fragment. The rapidity

dependence of $\langle p_x/M \rangle$, where M is the mass of the fragment, is then plotted as a function of the rapidity and is considered as a measure of the nuclear collective flow. Figures 21 and 22 show the experimental and predicted rapidity dependence of $\langle p_x/M \rangle$ for protons and deuterons emitted in central and peripheral collisions. Figure 23 corresponds to tritons and $Z = 2$ nuclear fragments for which once again the statistics is not large enough to differentiate between central and peripheral collisions. Rapidity bins have been adjusted in order to have an identical statistical error in each bin.

Figure 21 shows that, for protons, the experimental values of $\langle p_x/M \rangle$, corresponding to large rapidities, are shifted toward higher absolute values when going from 400 to 800 MeV/nucleon reaction, but once again is quite insensitive to the impact parameter selection. This figure also indicates that, for protons emitted with a large positive or negative rapidity, the cascade-percolation model cannot reproduce the experimental values of $\langle p_x/M \rangle$.
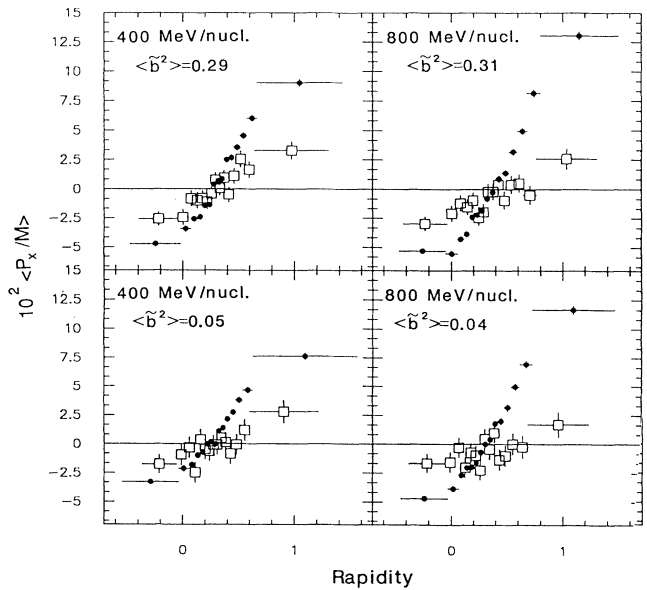

FIG. 21. $\langle p_x/M \rangle$ versus rapidity for protons emitted in central or peripheral 400 and 800 MeV/nucleon Ne+Nb collisions.

Figure 22 indicates that for deuterons emitted in peripheral collisions, while the experimental values of $\langle p_x/M \rangle$ at large positive or negative rapidities are still underpredicted by the cascade-percolation model, the experimental variation of $\langle p_x/M \rangle$ versus y is quite correctly reproduced for intermediate rapidities. A large discrepancy appears for deuterons emitted in central collisions, especially at 800 MeV/nucleon.

Figure 23 shows that the best agreement between the experimental and cascade-percolation predicted rapidity dependence of $\langle p_x/M \rangle$ occurs for $Z=2$ nuclear fragments emitted in a 400 MeV/nucleon reaction. One has to keep in mind that, for tritons and $Z=2$ nuclear fragments, the data are dominated by peripheral collisions.

For each species of light fragment, the variation of $\langle p_x/M \rangle$ versus rapidity can be characterized by two parameters, the center-of-mass rapidity y_0 of these particles and the flow parameter F, defined by

$$F = \left[\frac{\partial}{\partial y} \langle p_x/M \rangle \right]_{y=y_0} . \tag{17}$$

Since the number of baryons used in order to determine the reaction plane is limited, the estimated reaction plane differs from the true one: The less the multiplicity of baryons is, the larger the fluctuations of the estimated reaction plane around the true one are. Danielewicz and Odyniec [28] propose a correction on the average of this deviation which consists in the evaluation of the mean value of $\cos\Delta\phi$, where $\Delta\phi$ is the azimuthal deviation of the vector $\mathbf{Q}$ from the true reaction plane. This factor $\langle \cos\Delta\phi \rangle$ can be used afterwards in order to renormalize $\langle p_x/M \rangle$ and the flow parameter F since

FIG. 22. $\langle p_x/M \rangle$ versus rapidity for deuterons emitted in central or peripheral 400 and 800 MeV/nucleon Ne+Nb collisions.
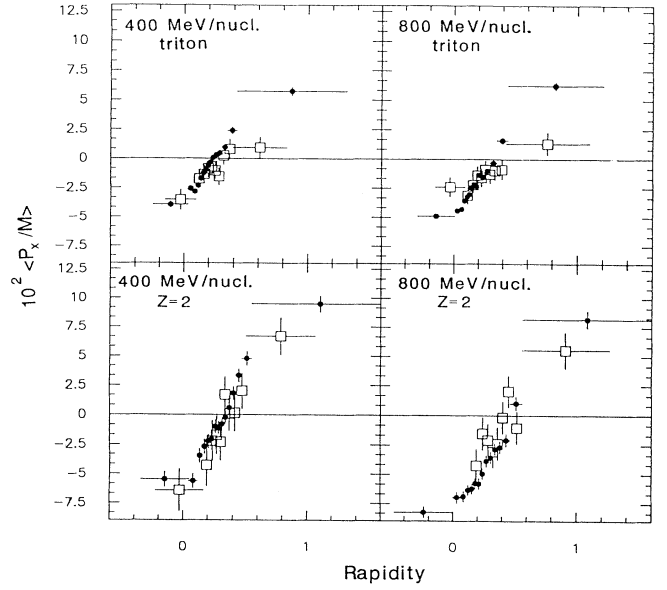

FIG. 23. $\langle p_x/M \rangle$ versus rapidity for tritons and $Z=2$ nuclear fragments emitted in 400 and 800 MeV/nucleon Ne+Nb collisions.

$$\langle p_x'/M \rangle = \frac{\langle p_x/M \rangle}{\langle \cos\Delta\phi \rangle} ,$$

$$F' = \left[\frac{\partial}{\partial y} \langle p_x'/M \rangle \right]_{y=y_0} = \frac{F}{\langle \cos\Delta\phi \rangle} , \tag{18}$$

where $\langle p_x'/M \rangle$ is the mean value of the transverse momentum projected onto the true reaction plane. The experimental and predicted values of the two parameters F and y_0, and $\langle \cos\Delta\phi \rangle$ calculated from p, d, t, and $Z=2$ nuclear fragments are summarized in Table VI. The two parameters F and y_0 have been extracted from a fit of the rapidity dependence of $\langle p_x/M \rangle$ without the two extreme values corresponding to the largest positive or negative rapidities.

At each incident energy and for a given impact parameter range of the collision, experimental y_0 values are roughly equal for protons and deuterons. These experimental values also indicate that the center-of-mass rapidity is systematically shifted toward higher values when going from 400 to 800 MeV/nucleon. A similar increase is observed for protons and deuterons, when going to a more central reaction. The cascade-percolation predicted y_0 values are systematically larger, but are affected by such large errors that conclusions derived from then could be unreliable.

At 800 MeV/nucleon, the experimental flow parameter is quite independent of the impact parameter range of the reaction or of the nature of the particle. At 400 MeV/nucleon, the experimental values are shifted toward higher values when going from central to peripheral reactions or when going from tritons to $Z=2$ nuclear fragments. As a conclusion, the experimental values of the flow parameter F are not reproduced by the cascade-percolation predictions. The best agreement occurs only at 400 MeV/nucleon and for the $Z=2$ nuclear fragments.
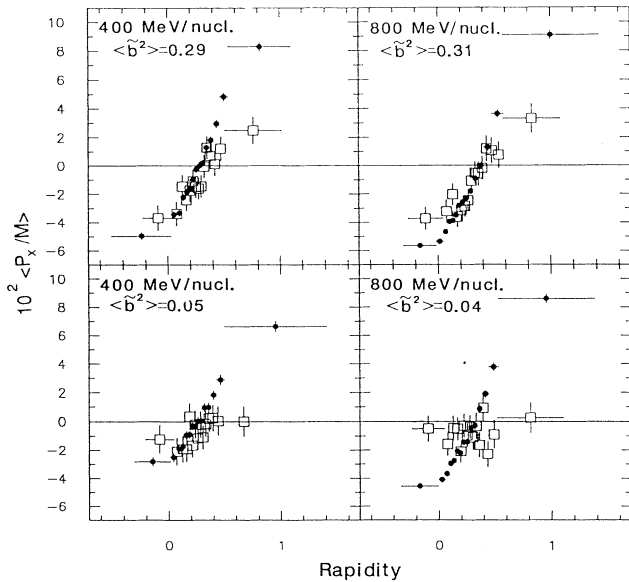
TABLE VI. Experimental and predicted center-of-mass rapidity (y_0), flow parameter (F), and $\langle \cos\Delta\phi \rangle$ as defined in Eqs. (16) and (17) and determined from transverse momentum analysis using p, d, t, and $Z = 2$ nuclear fragment emission in Ne+Nb 400 and 800 MeV/nucleon reactions. The errors in these parameters are indicated in parentheses. At 800 MeV/nucleon, the statistical uncertainty of the predicted value for deuterons is too large to permit a meaningful fit of the data. In order to have a sufficient statistic, there is no impact parameter selection for the analysis of tritons and $Z = 2$ nuclear fragments.

	E/A MeV	$\langle \tilde{b}^2 \rangle$	INC y_0	F	$\langle \cos\Delta\phi \rangle$	Expt. y_0	F	$\langle \cos\Delta\phi \rangle$
p	400	0.29	0.295 (0.057)	6.6 (0.9)	0.34	0.275 (0.019)	16.7 (0.7)	0.46
		0.05	0.367 (0.158)	3.2 (1.0)	0.30	0.229 (0.019)	12.2 (0.6)	0.44
	800	0.31	0.564 (0.150)	3.8 (0.9)	0.35	0.356 (0.024)	17.1 (0.8)	0.51
		0.04	0.650 (0.412)	2.1 (1.1)	0.20	0.290 (0.021)	15.8 (0.7)	0.54
d	400	0.29	0.355 (0.053)	10.6 (1.2)	0.34	0.274 (0.016)	18.2 (0.8)	0.45
		0.05	0.371 (0.132)	6.5 (1.9)	0.30	0.250 (0.016)	12.3 (0.5)	0.44
	800	0.31	0.418 (0.062)	10.6 (1.2)	0.35	0.369 (0.022)	16.0 (0.8)	0.50
		0.04				0.303 (0.020)	16.1 (0.8)	0.54
t	400		0.321 (0.083)	10.5 (2.1)	0.34	0.242 (0.016)	15.6 (0.8)	0.46
	800		0.434 (0.094)	7.0 (1.4)	0.33	0.317 (0.020)	15.5 (0.9)	0.50
$Z=2$	400		0.355 (0.060)	24.2 (2.8)	0.34	0.321 (0.026)	22.3 (1.3)	0.46
	800		0.473 (0.260)	12.2 (5.3)	0.33	0.531 (0.046)	16 (1.2)	0.50

V. DISCUSSION

In this paper we present a simple model for the prediction of some experimental observables concerning the production of protons and light nuclear fragments emitted in the DIOGENE acceptance for 400 and 800 MeV/nucleon Ne+Nb reactions. The main assumption of this model is that the reaction could be decomposed into two main stages. First is a violent interaction phase that begins with the interpenetration of the target nucleus by the projectile nucleus. During this phase, the initial longitudinal energy of the projectile nucleus is converted to thermal and compression energies for the system of "participant" nucleons. After reaching high temperature and density, the system expands and cools down toward lower density and temperature. Then the second stage of the reaction begins at the so-called "freeze-out" time (t_{FO}), when the remaining baryon-baryon collisions do not change drastically the phase space distribution. At this time, we suppose that nuclear fragments are suddenly formed by percolation of the nucleons in r space. So light nuclear fragment production is clearly dependent on the phase space distribution at the "freeze-out" time, which is directly fixed by the dynamic of the collision during the early phase. The dynamical treatment used to describe this first stage is the Liège intranuclear cascade model. The intranuclear cascade is calculated until a large final time ($t_F = 50$ fm/c), when the momentum distribution of the nucleons does not change anymore. As a matter of fact, the percolation should be done at the "freeze-out" time, but concretely this percolation is achieved at the final time of the cascade calculation. Nevertheless, the Liège cascade code presents the great advantage of recording for each event the whole history of the reaction. It is used afterwards to define, for each impact parameter configuration, T_{FO} as the time when the cumulated number of baryon-baryon collision reached the $\frac{2}{3}$ of its final value at the end of the reaction. The percolation radius at t_F is calculated for each specific impact parameter, using Eq. (2). The basic ingredients of this expression are the percolation radius at t_{FO}, r_d, and the maximum relative momentum of the nucleons inside a fragment, p_0. The value of p_0 is adjusted so as to get the best agreement between the experimental and theoretical cluster-to-proton ratios (d/p, t/p, and ^{3,4}He/p). Using a t_{FO} value of the order of 20 fm/c and the adjusted p_0 values, Eq. (2) gives r_{per} values at t_F equal to 9 fm/c (10 fm/c) for 400 (800) MeV/nucleon reactions.

Microscopic models had been used many times to calculate the initial conditions before the fragmentation phase in heavy-ion reactions, especially in asymmetric collisions in order to study the fragmentation of the excited projectile "spectator" system. We can quote as examples the study of the fragmentation of gold projectiles with the Boltzmann-Uehling-Uhlenbeck (BUU) model [29] or the comparison of QMD predictions with fragmentation data in a Ne+Au reaction at 1.05 GeV/nucleon [12]. In these calculations, the percolation is achieved at a very large final time $t_F = 300$ fm/c for the QMD predictions of Ne+Au reactions at 1.05 GeV/nucleon [12], and as shown by comparison between the experimental and the predicted fragment distributions, a percolation and radius equal to 3 fm seem to be adequate for the definition of the target "spectator" system. But in the present study the light nuclear fragments measured in the PDC acceptance are mainly formed from "participant" nucleons, and calculations using QMD [30] had shown that the experimental cluster-to-proton ratios (d/p, t/p, and ^{3,4}He/p) measured in the DIOGENE acceptance for 400 and 800 MeV/nucleon Ne+Nb reactions cannot be reproduced using a 3-fm percolation radius.

Our clusterization model is a considerable simplification of the real process of fragment formation that takes place during the deexcitation-expansion phase. But it has the advantage of adjusting by way of Eq. (2) the percolation radius to the percolation time. Some ingredients of the model could certainly be improved. First, we have to keep in mind that only "participant" nucleons are used in the model and that we define these "participant" nucleons in a very crude way as nucleons which underwent at least one collision. On the other hand, the experimental differentiation of measured fragments as issued from the "participant" nucleons source is not an easy job. This is done usually by way of a large energy cut. In our case the PDC acceptance is certainly sufficient for p and $Z = 2$ nuclear fragments; but when going to d and t, we measured much lower transverse momentum per nucleon fragments for which this differentiation is certainly more ambiguous.

Then we certainly need a more accurate evaluation of the original excitation energy of the primordial clusters before their deexcitation-evaporation phase. As an example, the percolation procedure generates filamented clusters and we could restructure these clusters as done in the model of Ngô et al. [6].

Nevertheless, our cascade-percolation picture is a rather successful one since the model reproduces quite well global experimental observables such as protons and light nuclear fragment total production cross sections (Table V) or multiplicity distributions (Figs. 6 and 7). It is not so surprising since the determination of p_0 is achieved so as to get the best agreement between the global experimental and theoretical cluster-to-proton ratios (d/p, t/p, and ^{3,4}He/p). But our model has some predictive power since the total nuclear charge multiplicity dependence of these cluster-to-proton ratios measured in the PDC acceptance is also rather nicely correctly reproduced (Fig. 8).

As a matter of fact, such global observables are more or less insensitive to the details of the forces that determine the dynamic of the reaction during the first stage. The situation is quite different for the description of more sophisticated dynamical observables.

The influence of the effective nucleon-nucleon cross sections on the dynamics of the reaction can most clearly be seen from the mean free path of the nucleons, i.e., the nuclear stopping power. So we compared the experimental rapidity distributions of the light nuclear fragments detected in the PDC acceptance to the corresponding predicted distributions: The best agreement occurs for peripheral collisions (Figs. 11 and 12).

For central collisions, only proton 800 MeV/nucleon experimental and predicted distributions show some agreement. These comparisons indicate that the degradation of the initial longitudinal momentum of the projectile nucleons by the target nucleons is not correctly reproduced by the cascade. A very important quantum feature of a heavy-ion collision is the Pauli blocking of the final states. At intermediate bombarding energies, the Pauli blocking factor $(1-f)$ causes a substantial reduction of the number of nucleon-nucleon collisions. However, this quantum feature and nonequilibrium effects lead to

different results in nuclear collisions: The mean free path λ increases due to the Pauli principle and decreases because of the high nuclear density. This is of drastic importance for the thermalization and the stopping power.

For a peripheral collision where the mean number of participant nucleons is reduced, the dynamic of the collision is more comparable with a succession of binary nucleon-nucleon collisions as done in the cascade model.

Nevertheless, one can quote that even at 400 MeV/nucleon, the experimental rapidity distributions are not at all consistent with the "fireball" process where all the initial longitudinal momenta would be converted to thermal energy.

Then we have looked on more sensitive observables as double-differential production cross sections, displayed with two independent variables y and $\gamma_\perp$. Using such sophisticated observables, one is often confronted with the problem of an insufficient sample of predicted events in order to infer information on the dynamic of the reaction. In the present case, it was impossible for these observables to differentiate between central or peripheral collisions. For protons, the 400 MeV/nucleon predicted distribution agrees with the experimental one except for some points corresponding to large $\gamma_\perp$ and y values ($\gamma_\perp \geq 1.4$, $y \geq 0.4$) and confirms what could be observed in Fig. 9 for the global rapidity distribution.

On the other hand, the plot of T_{eff} versus rapidity for protons at 800 MeV/nucleon indicates that, if the global rapidity distribution is correctly predicted by the model, T_{eff} (the slope of the $\gamma_\perp$ spectra in each rapidity bin) is quite significantly overpredicted by the cascade for the extreme rapidity values ($y \geq 0.6$ and $y \leq 0.1$). As claimed above, in-medium effects could have a large influence on the observables since the Pauli principle blocking of the final states leads to the reduction of the nucleon-nucleon scattering cross section in nuclear matter. That is what is done in the intranuclear model, but in Dirac-Brueckner theory [31] the nucleon-nucleon scattering also includes Pauli blocking of the intermediate states. This leads to an additional and non-negligible reduction of the effective nucleon-nucleon cross section, depending on the nuclear density reached during the reaction [$\sigma_{\text{eff}}/\sigma_{\text{free}}(p = 0.85$ GeV/$c)=0.7$ for $\rho/\rho_0=1$ and $\sigma_{\text{eff}}/\sigma_{\text{free}}(p = 0.85$ GeV/$c)=0.8$ for $\rho/\rho_0=2$]. That means that the distributions obtained with and without in-medium cross sections should exhibit a clear increase of "transparency" when in-medium cross sections are switched on.

It is a complete inverse situation that appears in Fig. 15 for the $Z = 2$ nuclear fragment 800 MeV/nucleon distribution: Low $\gamma_\perp$ values of the experimental distribution disagree with the predicted ones, so that the global rapidity distributions are simply shifted (Fig. 11). Nevertheless, the slopes at large $\gamma_\perp$ of the two distributions are roughly equivalent. ^{4}He emission is one of the decay channels of the large clusters of nucleons in the evaporation phase, so that an artificial excess of low-$\gamma_\perp$ $Z = 2$ nuclear fragments at these large rapidities indicates that the predicted phase space density for large rapidities is larger than the real one. Such a phenomenon is certainly enhanced if the excitation energy of prefragments is not

correctly evaluated by the model.

Since the product $T_{eff}N_{eff}$ is constant for the emission from a single Boltzmann source, we test the thermalization of the "participant" source from proton extracted parameters. The experimental product, as well as the predicted one, is not constant for both 400 and 800 MeV/nucleon reactions (Fig. 20).

Finally, we compared the experimental and predicted directed collective sideward emissions using the rapidity dependence of $\langle p_x/M \rangle$ calculated for a specific impact parameter range of the reaction and for each species of light nuclear fragment (p, d, t, and $Z=2$ nuclear fragment). This is of great importance since the magnitude of this transverse flow depends sensitively on the nuclear matter viscosity (effective nucleon-nucleon cross sections) and on the generalized equation of state (optical potential U). Comparison between the experimental data and the predictions points out again that the model lacks an important fraction of the proton sideward flow since experimental and predicted flow parameters (F) are not compatible. For heavier nuclear fragments, conclusions are not so clear since one can conclude that the agreement is better for $Z=2$ nuclear fragments. But the flow of the $Z=2$ nuclear fragments may result from an increased yield of low transverse momentum ^{4}He emission at high rapidity.

So, in conclusion, the cascade-percolation predictions reproduce quite well the main features of the reaction, as shown by comparison with the experimental global observables. For more sensitive experimental observables, comparisons with DIOGENE data confirm that the intranuclear cascade, although being a microscopic approach, gives a too small collective flow and insufficient nuclear stopping power.

But we believe that our approach, even if the clusterization recipe is a simple one, could be very fruitful in order to extract information on the first stage of the reaction. As the different steps of the model are relatively uncorrelated, such an approach is easy to extend to other models [QMD, BUU, and Vlasov-Uehling-Uhlenbeck (VUU)] that could calculate the nucleon phase space distribution after the compression stage of the reaction and predict the production of light nuclear fragments emitted at large angles. The main key of success is a simultaneous multiobservable analysis to constrain models (but for that we need a sufficiently large sample of simulated events). Another crucial point is also to perform a better selection of the impact parameters of the collision as done in the present study by only using the protonlike multiplicity.

[1] P. J. Siemens and J. I. Kapusta, Phys. Rev. Lett. **43**, 1486 (1979).

[2] G. Bertsch and J. Cugnon, Phys. Rev. C **24**, 2514 (1981).

[3] H. Stöcker, G. Buchwald, G. Graebner, P. Subramanian, J. A. Maruhn, W. Greiner, B. V. Jacak, and G. D. Westfall, Nucl. Phys. **A400**, 63c (1983); D. Hahn and H. Stöcker, *ibid.* **A476**, 718 (1988); Phys. Rev. C **37**, 1048 (1988).

[4] S. Das Gupta, Nucl. Phys. **A471**, 417c (1987).

[5] J. Desbois, Nucl. Phys. **A466**, 724 (1987); J. Nemeth, N. Barranco, J. Desbois, and C. Ngô, Z. Phys. A **325**, 347 (1986); J. Desbois, R. Boisgard, C. Ngô, and J. Nemeth, *ibid.* **328**, 101 (1987).

[6] C. Ngô, H. Ngô, S. Leray, and M. E. Spina, Nucl. Phys. **A499**, 148 (1989); F. Ighezou, C. Ngô, H. Ngô, S. Leray, and Y. M. Zheng, Phys. Lett. B **233**, 48 (1989); H. Ngô, C. Ngô, F. Ighezou, J. Desbois, S. Leray, and Y. M. Zheng, Z. Phys. A **337**, 81 (1990); C. Ngô,H. Ngô, S. Leray, and M. E. Spina, Nucl. Phys. **A511**, 414 (1990).

[7] C. Grégoire, B. Remaud, F. Sebille, L. Vinet, and Y. Raffray, Nucl. Phys. **A465**, 317 (1987).

[8] S. Leray, C. Ngô, P. Bouissou, B. Remaud, and F. Sebille, Nucl. Phys. **A531**, 177 (1991).

[9] J. Cugnon and C. Volant, Z. Phys. A **324**, 435 (1989).

[10] A. S. Botvina, A. S. Iljinov, and I. N. Mishutin, Nucl. Phys. **A507**, 649 (1990).

[11] J. Aichelin and H. Stöcker, Phys. Lett. B **176**, 14 (1986); S. M. Kiseleev, *ibid.* **198**, 324 (1987); G. Peilert, A. Rosenhauer, H. Stöcker, and W. Greiner, Mod. Phys. Lett. A **3**, 459 (1988).

[12] J. Aichelin, G. Peilert, A. Bohnet, A. Rosenhauer, H. Stöcker, and W. Greiner, Phys. Rev. C **37**, 2451 (1988).

[13] G. Montarou, J. P. Alard, J. Augerat, L. Fraysse, M. J. Parizet, R. Babinet, Z. Fodor, J. Girard, J. Gosset, C. Laspalles, M. C. Lemaire, D. L'Hôte, B. Lucas, J. Poitou, W. Schimmerling, Y. Terrien, F. Brochard, P. Gorodetzky, C. Racca, J. Cugnon, and J. Vandermeulen, Phys. Rev. C **44**, 365 (1991).

[14] J. Cugnon, Phys. Rev. C **23**, 2094 (1981); J. Cugnon, D. Kinet, and J. Vandermeulen, Nucl. Phys. **A379**, 553 (1982).

[15] V. Kevin and M. Whitney, Commun. ACM **15**, 273 (1972).

[16] C. M. Lederer and V. S. Shirley, *Table of Isotopes* (Wiley, New York, 1978).

[17] G. Fai, J. Randrup, Nucl. Phys. **A381**, 557 (1982); **A404**, 551 (1983).

[18] J. P. Alard, J. P. Arnold, J. Augerat, R. Babinet, N. Bastid, F. Brochard, J. P. Costilhes, M. Crouau, N. De Marco, M. Drouet, P. Dupieux, H. Fanet, Z. Fodor, L. Fraysse, J. Girard, P. Gorodetzky, J. Gosset, C. Laspalles, M. C. Lemaire, D. L'Hôte, B. Lucas, G. Montarou, A. Papineau, M.-J. Parizet, J. Poitou, C. Racca, W. Schimmerling, J. C. Tamain, Y. Terrien, J. Valéro, and O. Valette, Nucl. Instrum. Methods A **261**, 379 (1987).

[19] J. Poitou, Nucl. Instrum. Methods **217**, 373 (1983).

[20] C. Cavata, M. Demoulins, J. Gosset, M.-C. Lemaire, D. L'Hôte, J. Poitou, and O. Valette, Phys. Rev. C **42**, 1760 (1990).

[21] K. H. Kampert, J. Phys. G **15**, 691 (1989); H. Gutbrod, K. H. Kampert, B. W. Kolb, A. M. Poskanzer, H. G. Ritter, and H. R. Schmidt, Z. Phys. A **337**, 57 (1990).

[22] J. Gosset, H. H. Gutbrod, W. G. Meyer, A. M. Poskanzer, S. Sandoval, R. Stock, and G. D. Westfall, Phys. Rev. C **16**, 629 (1977).

[23] J. Gosset (unpublished).

[24] *Handbook of Mathematical Functions,* edited by M. Abramowitz and I. Stegun (Dover, New York, 1970).

[25] G. F. Chapline, M. H. Johnson, E. Teller, and M. C.

Weiss, Phys. Rev. D **8**, 4302 (1973); W. Scheid, H. Müller, and W. Greiner, Phys. Rev. Lett. **21**, 741 (1974).

[26] H. Stöcker, J. A. Maruhn, and W. Greiner, Z. Phys. A **293**, 173 (1979); H. Stöcker, G. Graebner, J. A. Maruhn, and W. Greiner, Phys. Lett. **95B**, 1982 (1980); H. Stöcker, J. A. Maruhn, and W. Greiner, Phys. Lett. **44**, 725 (1980); H. Stöcker, R. Y. Cusson, G. Graebner, J. A. Maruhn, and W. Greiner, Z. Phys. A **294**, 125 (1980); G. Buchwald, G. Graebner, J. Theis, J. A. Maruhn, W. Greiner, H. Stöcker, K. Frankel, and M. Gyulassy, Phys. Rev. C **28**, 2349 (1983).

[27] H. H. Gutbrod, K. H. Kampert, B. Kolb, A. M. Poskanzer, H. G. Ritter, and H. R. Schmidt, Phys. Lett. B **216**, 1207 (1989); H. H. Gutbrod, K. H. Kampert, B. Kolb, A. M. Poskanzer, H. G. Ritter, R. Schicker, and H. R. Schmidt, Phys. Rev. C **42**, 460 (1990); M. Demoulins, D. L'Hôte, J. P. Alard, J. Augerat, R. Babinet, N. Bastid, F. Brochard, C. Cavata, N. De Marco, P. Dupieux, H. Fanet, Z. Fodor, L. Fraysse, P. Gorodetzky, J. Gosset, T.

Hayashino, M. C. Lemaire, A. Le Merdy, B. Lucas, J. Marroncle, G. Montarou, M. J. Parizet, J. Poitou, D. Qassoud C. Racca, W. Schimmerling, Y. Terrien, and O. Valette, Phys. Lett. B **241**, 476 (1990).

[28] P. Danielewicz and G. Odyniec, Phys. Lett. **157B**, 146 (1985); P. Danielewicz, H. Ströbele, G. Odyniec, D. Bangert, R. Bock, R. Brockmann, J. W. Harris, H. G. Pugh, W. Rauch, R. E. Renfordt, A. Sandoval, D. Schall, L. S. Schroeder, and R. Stock, Phys. Rev. C **38**, 120 (1988); M. Demoulins, Ph.D. thesis, Université Paris-sud, 1989.

[29] C. Ogilvie *et al.*, Phys. Rev. Lett. **67**, 1214 (1991); P. Hubele *et al.*, Z. Phys. A **340**, 263 (1991).

[30] J. Marroncle, Ph.D. thesis, Université Clermont II, 1989.

[31] R. Malfliet, in *Proceedings of the NATO Workshop on Nuclear Matter and Heavy Ion Collisions*, Vol. 205 of *NATO Advanced Study Institute, Series B: Physics*, edited by M. Soyeur, H. Flocard, B. Tamain, and M. Porneuf (Plenum, New York, 1989), p. 73.